Chromatin dynamics are constrained by loops and driven by the INO80 nucleosome remodeler

Mary Lou P. Bailey[1,2]*, Ivan Surovtsev[3,4]*, Jessica F. Williams[4]*, Hao Yan[2,3]*, Tianyu Yuan[3], Simon G. J. Mochrie[1,2,3 #] and Megan C. King[2,4,5 #]

[1] Department of Applied Physics, Yale University, New Haven, Connecticut 06511, USA
[2] Integrated Graduate Program in Physics Engineering Biology, Yale University, New Haven, Connecticut 06511, USA
[3] Department of Physics, Yale University, New Haven, Connecticut 06511, USA
[4] Department of Cell Biology, Yale School of Medicine, New Haven, Connecticut 06520, USA
[5] Department of Molecular, Cell and Developmental Biology, Yale University, New Haven, Connecticut 06511, USA

* equal contributions
# correspondence to simon.mochrie@yale.edu or megan.king@yale.edu

Abstract

The chromosomes - DNA polymers and their binding proteins - are compacted into a spatially organized, yet dynamic, three-dimensional structure. Recent genome-wide chromatin conformation capture experiments reveal a hierarchical organization of the DNA structure that is imposed, at least in part, by looping interactions arising from the activity of loop extrusion factors. The dynamics of chromatin reflects the response of these polymers to a combination of thermal fluctuations and active processes. However, how chromosome structure and enzymes acting on chromatin together define its dynamics remains poorly understood. To gain insight into the structure-dynamics relationship of chromatin, we combine high-precision microscopy in living *Schizosaccharomyces pombe* cells with systematic genetic perturbations and Rouse-model polymer simulations. We first investigated the model that the activity of two loop extrusion factors, cohesin and condensin, drives chromatin dynamics. Surprisingly, deactivating cohesin or condensin increased chromatin mobility, suggesting that loop extrusion constrains rather than agitates chromatin motion. Our corresponding simulations reveal that the introduction of loops is sufficient to explain the constraining activity of loop extrusion factors, highlighting that the conformation adopted by the polymer plays a key role in defining its dynamics. We also find that the activity of the INO80 chromatin remodeler, but not the SWI/SNF or RSC complexes, is critical for ATP-dependent chromatin mobility in fission yeast. Taken together we suggest that thermal and INO80-dependent activities exert forces that drive chromatin fluctuations, which are constrained by the organization of the chromosome into loops.

Introduction

Chromatin, which is comprised of DNA and its associated proteins, is confined within the cell nucleus of eukaryotes, where it takes on a compartmentalized, three-dimensional structure. While we understand the molecular details of nucleosomes, the fundamental unit of chromatin, only recently has a unified model for the intermediate scale of chromatin organization emerged, namely the existence of topologically associating domains (TADs). 100 kb to Mb scale TADs are now considered to be a characteristic unit of mesa-scale chromosomal folding, revealed largely through genome-wide chromosome conformation capture techniques (e.g., Hi-C) (Dekker, 2014; Dixon et al., 2016; Dixon et al., 2012; Mizuguchi et al., 2014; Nora et al., 2012; Sexton et al., 2012).

The structure of TADs is thought to arise through characteristic chromatin looping interactions. The major molecular machinery responsible for chromatin loops is composed of members of the structural maintenance of chromosome (SMC) complex family of ATPases, most notably in the form of the cohesin and condensin complexes (Banigan and Mirny, 2020). Indeed, high levels of cohesin and condensin reside at boundaries between TADs at steady-state (Mizuguchi et al., 2014; Nora et al., 2012). Given the established ability of SMC complexes to topologically engage DNA strands (Haering et al., 2008; Terakawa et al., 2017), it has been widely suggested that SMC complexes are loop extrusion factors (LEFs) that drive the formation of chromatin loops, an activity that can be observed *in vitro* or in extracts (Davidson et al., 2019; Ganji et al., 2018; Golfier et al., 2020; Kim et al., 2019). Moreover, loss of functional cohesin in fission yeast leads to a complete loss of TADs as assessed by Hi-C through a mechanism distinct from its role in sister chromatid cohesion (Mizuguchi et al., 2014) while complete depletion of cohesin similarly leads to the loss of TADs in mammalian cells (Rao et al., 2017). LEF simulations further demonstrate that the dynamic extrusion of loops by SMC complexes combined with the existence of boundary elements encoded in the DNA (for example, sequence-specific binding of CTCF, which is enriched at boundaries and physical interacts with cohesin (Parelho et al., 2008; Wendt et al., 2008), can give rise to contact maps similar to those revealed experimentally through Hi-C (Banigan et al., 2020; Fudenberg et al., 2016; Nuebler et al., 2018). Consistent with the LEF model, recent experimental studies demonstrate that cohesin and condensin can actively drive loop formation on naked DNA (Davidson et al., 2019; Ganji et al., 2018; Haarhuis et al., 2017; Kim et al., 2019). Taken together, these observations suggest that cohesin and condensin are ATP-dependent drivers of dynamic DNA looping.

From a functional perspective, TADs play a critical role in defining the probability of physical contacts along the chromosome; these units correlate with chromatin attributes such as gene expression levels, suggesting that form and function of TADs are intricately linked (Ibrahim and Mundlos, 2020). It is intuitive that genetic transactions requiring interactions between DNA elements will be influenced by both TAD structure and dynamics. For example, discrete chromatin contacts that underlie critical regulatory processes such as transcriptional enhancement and co-regulation are tied to cohesin function, as is insulation and the suppression of genomic interactions with undesirable outcomes (Flavahan et al., 2016; Lupianez et al., 2015; Nora et al., 2012; Shen et al., 2012; Symmons et al., 2014). However, the static, time-averaged view of TADs arising from Hi-C models derived from thousands of cells fails to address the underlying chromatin dynamics on which TADs impinge. Moreover, in-situ hybridization approaches that can be applied to individual, fixed cells (Bintu et al., 2018; Wang et al., 2016) also cannot address how chromatin folding influences its dynamics. Indeed, how TADs, and the formation or persistence of looping interactions on which they depend, impact the dynamic properties of chromatin *in vivo* is largely unknown.

The chromosomes behave as large polymers that are crowded within the nuclear volume. Given that individual genetic loci are part of these large chromosomes and move through the crowded nucleoplasm, it is not surprising that they display a characteristic sub-diffusive behavior across model systems (Heun et al., 2001; Marshall et al., 1997; Weber et al., 2012). An unusual aspect of chromatin mobility is its apparent dependence on cellular energy (Heun et al., 2001; Joyner et al., 2016; Marshall et al., 1997; Weber et al., 2012). A persistent mystery is the identity of the energy-dependent process(es) underpinning this observation and whether it reflects changes to the material properties of the nucleoplasm upon energy depletion (Joyner et al., 2016) and/or a role for ATP-requiring enzyme activities in driving chromatin dynamics. Given that SMC proteins are themselves ATPases capable of driving chromatin looping interactions, they represent such possible factors.

Here we employ a combination of live cell imaging of gene loci in fission yeast with polymer dynamics simulations to investigate how the configuration (specifically TADs) and dynamics of chromatin are linked. On short (seconds) timescales we find that most gene loci in fission yeast display highly similar dynamical properties regardless of location on the chromosome. Surprisingly, we find that loss of either cohesin or condensin function increases chromatin locus fluctuations, suggesting that chromatin loops made by SMC complexes predominantly constrain

chromatin movement rather than driving chromatin dynamics through the act of loop extrusion. Employing Rouse-polymer simulations we independently show that chromatin looping interactions constrain chromatin mobility in a manner that recapitulates our experimental data. Lastly, we identify the INO80 complex as an important driver of chromatin mobility, a role specific to the INO80 but not other ATP-dependent nucleosome remodelers. Taken together, we demonstrate that energy-dependent chromatin mobility is likely driven, at least in large part, by the action of INO80, while TADs introduce constraints on chromatin mobility.

Results

Chromatin loci show a characteristic sub-diffusive behavior in fission yeast at short time scales

To gain insights into the factors that contribute to dynamic chromatin organization *in vivo*, we developed a live-cell imaging, tracking, and analysis approach to precisely characterize the spatial and temporal dynamics of chromatin loci at short (ms-s) timescales (Fig. 1a). We visualized chromosomal loci dynamics in fission yeast by both targeted and random integrations of *lac* operator (*lacO*) repeats and expression of fluorescently-tagged *lac* repressor (GFP-LacI). Widefield fluorescence microscopy movies are obtained at short (58 ms) timesteps. We apply a single particle tracking (SPT) algorithm that performs a Gaussian fit on the diffraction-limited *lacO*/GFP-LacI focus to define its position, which we track over time. Thousands of individual particle tracks are then subjected to motion analysis by calculating and theoretically fitting the mean squared displacement (MSD) versus time from (Bailey et al., 2021). Covariance analysis of the particle tracks further revealed that the motion of gene loci in fission yeast can be described by a single diffusive state (Bailey et al., 2021). On the seconds timescale we observe a characteristic sub-diffusive behavior in fission yeast that is nearly identical at six different genomic positions (Fig. 1b and Figure 1-figure supplement 1a). On these timescales this characteristic chromatin motion is well described by a single mean anomalous exponent (α=0.44 $\pm$ 0.02), which provides a good description for all experimental MSDs for the first 29 time points (between 0.058 and 1.7 s) as indicated by the fit (solid lines) to the anomalous diffusion equation (Eq. 1, see Methods). Of note, this value is slightly but consistently lower than that predicted for an ideal Rouse polymer of α=0.5 (Doi and Edwards, 1986), which is the value previously ascribed to the dynamics of budding yeast chromatin (Weber et al., 2012). Indeed, using our pipeline we also recapitulate a value close to α=0.5 for budding yeast harboring a tagged chromatin locus (Figure 1-figure supplement 1b), suggesting that the depressed value we observe in fission yeast is likely meaningful (see below). Applying an exponent of α=0.44, the “diffusion coefficient’’, D, ranges from 0.0025 – 0.0031 $\mu m^2/s^{0.44}$ across the six genetic loci in fission yeast (see Supplemental Table S1). Consistent with prior studies, depletion of ATP by the addition of sodium azide decreases the diffusivity about two-fold (from 0.0028 to 0.0015 $\mu m^2/s^{0.44}$ for the *mmf1* locus (Fig. 1c)).

Microtubule-driven centromere oscillations influence chromatin dynamics on longer time scales

In fission yeast, centromeres are mechanically coupled to the spindle pole body (SPB; the centrosome equivalent) (Funabiki et al., 1993). Thus, forces from microtubule polymerization that drive oscillation of the SPB along the long axis of the cell on the minutes timescale (Tran et al., 2001) could manifest in chromatin motion, even in regions distal to the centromere. Indeed, over tens of seconds we observe clear super-diffusive behavior (α>1) for a *lacO* integration directly adjacent to the centromere (*cen2*) (Fig. 2a). This behavior is dependent on microtubules as their depolymerization with carbendazim (MBC) leads to a strong depression of motion at *cen2* and the adoption of sub-diffusive behavior (Fig. 2a). Although more subtle, we also observe that the *mmf1* locus (~ 1.8. Mb from the centromere) is more diffusive in the presence of intact microtubule dynamics (Fig. 2a, apparent after time delays of ~5s). We exclude that this effect is due to rigid body movement of the nucleus due to microtubules forces exerted on the SPB on this timescale (Figure 2-figure supplement 1). Interestingly, below the ~5 second time delay regime *cen2* displays lower diffusivity than the *mmf1* locus (D=0.0016 $\mu m^2/s^{0.44}$ in the presence of MBC), suggesting that bridging centromeres to the SPB acts to constrain chromatin motion at short times. Indeed, if we focus on the same time regime explored in Fig. 1 (up to a time delay of ~4s), microtubule dynamics play a minor role on the diffusivity of *cen2*, which is far more constrained than *mmf1* (Fig. 2b). At *mmf1* we observe only a nominal contribution of microtubule dynamics to the observed diffusivity at this time scale (D=0.0026 $\mu m^2/s^{0.44}$ in the presence of MBC, Fig. 2b). We chose to focus on this seconds time regime where there is little influence of microtubule dynamics for the rest of our study.

The loop extrusion complexes, cohesin and condensin, primarily constrain chromatin motion in fission yeast

Chromosome conformation depends on the activity of cohesin and condensin in fission yeast. Loss of cohesin strongly disrupts TADs as assessed by Hi-C (independent of its role in sister chromatid cohesion) (Mizuguchi et al., 2014) while condensin plays a more subtle but nonetheless discernible role in interphase chromatin organization (Kakui et al., 2020). Condensin and cohesin presumably shape chromosomes through their loop extrusion activity, resulting in a dynamic steady state of DNA loops that appear and disappear in a stochastic fashion. However, to-date little experimental evidence addresses if and how the process of loop extrusion impacts chromatin mobility. Since DNA loop extrusion by cohesin and condensin requires ATP (Davidson et al., 2019; Ganji et al., 2018; Kim et al., 2019), LEF activity could underlie ATP-dependent chromatin motion; this model predicts that loss of cohesin and/or condensin function would therefore dampen chromatin dynamics. To test this hypothesis, we

examined how the motion of two loci, *mmf1* and *pfl5*, which are distant from the centromeres, were affected by loss of cohesin or condensin function. Specifically, we employed critical loss-of-function, temperature-sensitive alleles of the cohesin loading factor (*mis4-242*) or of the SMC2 subunit of condensin (*cut14-208*). To our surprise, we observed a profound increase in chromatin mobility (~30 to ~50% increase in the diffusion coefficient, D) upon loss of either LEF function at *mmf1* (Fig. 3a), with a greater effect upon disruption of cohesin loading. These effects of disrupting LEF function on the dynamics of the *pfl5* locus were qualitatively similar (Fig. 3b). These observations suggest that, on this time scale, cohesin and condensin loop-extruding activity constrains chromatin movement rather than drives chromatin mobility. Moreover, SMC complexes appear dispensable for the ATP-dependent chromatin mobility that we (and others) observe (Fig. 1c).

Simulations predict that looping interactions constrain chromatin mobility

To understand theoretically the potential impact of chromatin loops and loop extrusion on fluctuations of the chromatin polymer, we turned to modeling. We coupled LEF-model simulations of the dynamic loop configuration of specific genomic regions to Rouse-model polymer simulations. The best described model of chromatin organization by loop extrusion employs random loading of LEFs that extrude loops until they encounter another LEF or a boundary element, specifically a site bound by CTCF (Alipour and Marko, 2012; Fudenberg et al., 2016; Nuebler et al., 2018), or until the LEF dissociates, causing the loop to dissipate. As CTCF does not exist in fission yeast, we first applied such simulations to the mouse genome for which CTCF binding sites have been measured; these sites serve to constrain the loops. We described each 10 kb region of the mouse genome as a bead connected to its neighbors by springs of stiffness, k, and experiencing a friction coefficient, ζ. To incorporate loops, we augmented the usual nearest-neighbor Rouse model with additional springs (of the same spring constant) that connect non-adjacent beads, thus representing the base of a loop. The number of loops and their locations evolve according to the LEF model, incorporating LEFs and boundary elements, similar to that described by Mirny and colleagues (Fudenberg et al., 2016; Nuebler et al., 2018), with the result that there are typically 30 loops within a 6 Mbp region of the mouse genome. The MSD of each gene locus is then determined from the resultant time series of bead positions. We also carried out analogous classical Rouse model simulations without any loops.

The comparison of MSDs between the Rouse simulations without loops (red trace) and with CTCF-dependent loops (green trace) reveals that loops constrain chromatin motion (Fig. 4a),

consistent with our experimental MSD measurements of gene loci in *S. pombe* with and without disrupted SMC loading or activity (Fig. 2). Increased chromatin motion was tied to representative chromatin conformations that were less compact in the absence of loops (Fig. 4b, red) compared to the condensed conformations commonly sampled in response to LEF function and the resulting loops (Fig. 4b, green).

We next developed an analogous simulation approach that could be applied to the fission yeast genome. Yeasts lack CTCF, although they likely have alternative boundary elements that define experimentally observed TADs (Mizuguchi et al., 2014; Thon et al., 2002). We therefore devised a simulation, which we call the "LEF only" model, based on two concepts: 1) random loading of LEFs and 2) the ability of the LEF to move from its loading site until it encounters another LEF (or dissociates) – a feature of many loop extrusion models (Alipour and Marko, 2012; Fudenberg et al., 2016; Nuebler et al., 2018). Similar to the CTCF-dependent mouse genome results, we again observe that LEF activity leads to a reduction in the MSD (Fig. 4c) and more compact polymer conformations (blue, Fig. 4d, compare to without loops, red). Moreover, In addition, subjecting the mouse genome to this alternate loop extrusion simulation lacking CTCF-encoded boundaries also constrains the MSD (Fig. 4a-b, blue trace and polymer model). Thus, regardless of the particular LEF model implementation and the species of genome, the trend of constrained chromatin mobility in response to loop extrusion is maintained.

Loop extrusion decreases the effective exponent describing chromatin diffusivity

We next inquired whether the loop configuration simulations could provide further insight into our observation that the sub-diffusive chromatin motion in fission yeast displays an exponent, α, of ~0.44, which deviates from that expected for a Rouse polymer ($\alpha = 0.5$). To this end, we calculated the effective exponent, $\alpha = [\log MSD(t_{n+1}) - \log MSD(t_n)]/[\log t_{n+1} - \log t_n]$ from the simulated chromatin configurations and compared how α is influenced by loop extrusion in the simulations. As expected, the effective exponents for the classical Rouse model lacking loops lies close to 0.5 for the mouse simulations (Fig. 4e, red trace). Remarkably, however, the effective exponent in the presence of loop extrusion employing either the CTCF LEF model (Fig. 4e, blue trace) or the "LEF-only" model (Fig. 4e, green trace) shows a gently evolving value with a mean that appears to vary continuously from a value near $\alpha \simeq 1/2$ for $t \simeq \gamma$ to a value near $\alpha = 0.4$ for $t \simeq 10^3\gamma$. Similarly, loop extrusion depresses the value of the effective exponent in the fission yeast "LEF only" simulations (Fig. 4f). These results are strikingly reminiscent of our finding that experimental MSDs in *S. pombe* are well-described overall by a value of $\alpha \simeq 0.44$

(Fig. 1). Thus, our data support a model in which chromatin looping interactions manifest in decreased values for both the MSD and α.

The INO80 chromatin remodeler drives chromatin mobility in fission yeast

Both our experimental and simulation approaches find that loop extrusion by SMC complexes predominantly suppresses chromatin mobility. Nonetheless, there must be a force acting on the chromatin polymer to elicit its fluctuations. In principle, fluctuations and mobility might be of thermal origin. However, this is inconsistent with the effect of ATP depletion (Fig. 1c), which indicates an important role for processes tied to cellular metabolism. ATP-dependent chromatin (nucleosome) remodelers represent attractive alternative candidates for driving energy-dependent chromatin mobility. Whether this activity is also tied to LEF function, and more generally if and how nucleosomes impact on the translocation of LEFs along the DNA, remains incompletely understood. To test whether chromatin remodelers contribute to ATP-dependent chromatin mobility, we examined cells lacking Arp8, an auxiliary component of the essential INO80 remodeling complex, and Arp9, a component of both the SWR1 and RSC remodeling complexes. Strikingly, loss of Arp8 led to a clear suppression of chromatin mobility (D=0.0024 $\mu m^2/s^{0.44}$), representing a 40% decrease in the ATP-dependent diffusivity, i.e. above the basal, ATP-depleted motion; Fig. 5a). By contrast, loss of Arp9 had little effect (Fig. 5a). Importantly, as INO80 is essential for viability, Arp8 deletion is akin to a hypomorphic allele rather than a complete loss-of-function, leaving open the possibility that INO80 activity contributes to ATP-dependent chromatin diffusivity to an even greater extent than is observed in *arp8Δ* cells. These results are consistent with a prior study in which INO80 (but not SWR1 or RSC) was both required for a transcription-dependent boost in chromatin mobility and was sufficient to impart increased diffusivity when artificially targeted to a chromosomal locus in budding yeast (Neumann et al., 2012), although the unique role for INO80 but not SWR and RSC remains unexplained.

To address the interplay between the boosting of chromatin mobility by INO80 and the constraint imposed by LEFs, we examined how loss of Arp8 and the elevated chromatin diffusivity observed in LEF mutants would intersect. At short times at the permissive temperature the effect of Arp8 deletion dominates, displaying decreased diffusivity of the *mmf1* locus regardless of the state of *cut14*, although there is an upwards trend at longer times in cells harboring the *cut14-208* allele. At the non-permissive temperature, loss of Arp8 quantitatively dampens the elevated chromatin dynamics in the *cut14-208* background (Fig. 5b; D=0.0031

$\mu m^2/s^{0.44}$); the magnitude of the effect (a ~30% decrease of the ATP-dependent diffusivity; Fig. 5b) is only slightly smaller than that observed upon Arp8 deletion in WT cells or at the permissive temperature. Importantly, the level of absolute diffusivity in *cut14-208 arp8Δ* cells at the non-permissive temperature remains substantially elevated compared to cells lacking only Arp8 (D=0.0031 versus 0.0024 $\mu m^2/s^{0.44}$). Taken together, these observations suggest that 1) INO80 activity is a major driver of chromatin fluctuations in fission yeast and 2) loop extrusion influences the manner in which these fluctuations act on the chromatin polymer.

Discussion

Here we provide new insights into the relationship between chromosome structure and dynamics. Combining live cell imaging and polymer simulations we converge on the conclusion that chromatin loops, which arise by SMC-driven loop extrusion, primarily constrain chromatin mobility. This constraint manifests as a decrease in the MSD of chromatin loci and the effective exponent describing their sub-diffusive behavior. We provide evidence that the activity of the INO80 chromatin remodeler is a major source of the as-yet mysterious, energy-dependent activity that drives chromatin motion. Our findings emphasize that both the chromatin conformation and the molecular machines acting on that polymer together determine chromatin dynamics.

Loops as constraints to chromatin mobility

The formation of TADs, revealed by approaches such as Hi-C and fluorescence *in situ* hybridization (FISH), appears dependent on the activity of LEFs such as cohesin. Importantly, however, as these are techniques applied to fixed cells, Hi-C and FISH are not suitable to interrogate how loop extrusion and the presence of loops influence chromatin dynamics. Cohesin and condensin, both harboring ATPase activity, could easily be intuited to drive chromatin mobility. Thus, our observations that loop extrusion constrains chromatin mobility is, on the surface, surprising. The key finding is therefore that the major influence of chromatin loops is their effect on the chromatin polymer's fluctuations in response to force, mediated by effective springs at the base of loops that couple distant segments of the chromosome. Ultimately these additional constraints decrease chromatin mobility. This model has several ramifications. First, the ability of loops to constrain chromatin mobility could antagonize more distant, inter-TAD interactions, thereby reinforcing the relative over-representation of local, intra-TAD interactions. Second, loops are expected to disfavor longer-range, stochastic interactions, for example those that drive formation of compartments. Indeed, Hi-C studies demonstrate that LEFs (and the TADs they create) antagonize compartments (Gassler et al., 2017; Rao et al., 2017), suggesting that loss of loops leads to more unfettered contacts between self-associating chromatin landmarks, for example those driving B compartment cohesion (Falk et al., 2019). Lastly, an open question is to what extent the explicit position of a DNA element within a loop (for example, at the most distal portion of a loop versus at the loop base) restricts its mobility and therefore the complement of sampled interactions that can influence genetic transactions. If so, then the ability to remodel TADs or influence their lifetime could be highly influential on the outcome. Further studies will be required to precisely answer this open question. Importantly,

the influence of loops on the force response of the chromosome is independent of the specific mechanisms driving the position of TADs across eukaryotic models (e.g. organisms outside of bilateria that lack CTCF and/or employ other insulator proteins such as the widely conserved TFIIIC complex (Van Bortle and Corces, 2012)) and is therefore likely to play a fundamental and conserved role.

The ATP-dependence of chromatin mobility and nucleosome remodelers

The source of ATP-dependent chromatin mobility has been a perennial mystery, ever since the first live-cell recordings of chromatin dynamics were made using the *lacO*-LacI technology over twenty years ago (Heun et al., 2001; Marshall et al., 1997). Importantly, a study in budding yeast (and extended to fission yeast) demonstrates that caution must be exercised when interpreting experiments that disrupt cellular energy by glucose starvation, which results in altered cell volume, as this can lead to increased crowding that affects not just chromatin mobility but also other large macromolecular complexes (Joyner et al., 2016); for this reason, we have used sodium azide treatment to uncouple effects of ATP depletion from altered crowding in this study.

A renewed interest in actively-driven chromatin mobility has arisen through studies of the DNA damage response across multiple model systems (Zimmer and Fabre, 2019). Induction of a DNA double-strand break (DSB) not only leads to an increase in mobility of not only the broken chromosome region, but, surprisingly, also across the entire genome (Lawrimore et al., 2020; Miné-Hattab and Rothstein, 2013); this effect has been suggested to promote the homology search phase of DSB repair. While many factors contribute to this response, including nuclear and cytoplasmic cytoskeletal proteins (Caridi et al., 2018; Lawrimore et al., 2020; Lottersberger et al., 2015; Oshidari et al., 2018; Schrank et al., 2018; Swartz et al., 2014; Zhurinsky et al., 2019), of note the INO80 nucleosome remodeler appears to play a central role (Cheblal et al., 2020; Hauer et al., 2017; Neumann et al., 2012; Seeber et al., 2013). Indeed, in budding yeast loss of Arp8 disrupts the observed DSB-dependent boost in chromatin mobility (Cheblal et al., 2020; Hauer et al., 2017; Neumann et al., 2012; Seeber et al., 2013). Although the potential involvement of INO80 in multiple steps of DSB repair complicates the interpretation of the mechanisms at play, it nonetheless underscores the connection specifically between the INO80 nucleosome remodeler and chromatin dynamics, possibly due to INO80's role in nucleosome eviction (Cheblal et al., 2020).

Lastly, transcription has also been observed to drive a boost to chromatin dynamics across

model systems (Chuang et al., 2006; Gu et al., 2018; Neumann et al., 2012). Importantly, in budding yeast, the increase of chromatin mobility upon transcriptional activation again requires INO80 activity (Neumann et al., 2012). Further, in perhaps the most elegant demonstration of sufficiency, simply locally targeting INO80 to a *lacO* array is sufficient to recapitulate the transcription-driven boost in chromatin mobility even in the absence of transcription; this is not the case for other nucleosome remodeling complexes when similarly targeted (Neumann et al., 2012). Thus, a common theme is that a unique function of INO80 among nucleosome remodeling complexes lies at the heart of enhanced chromatin motion in response to DSBs or transcriptional activation. Our observations suggest that a critical role for INO80 in promoting chromatin mobility extends beyond such specialized contexts and is instead generalizable, driving a component of the ATP-dependent motion characteristic of chromatin.

Crosstalk between loop extrusion, nucleosomes, and chromatin remodelers

The potential role that nucleosome remodelers play in facilitating loop extrusion remains to be fully investigated, as we are just beginning to define mechanistically how nucleosomes impact loading and translocation of cohesin and condensin, particularly in living mammalian cells. Single-molecule experiments show that nucleosomes impede cohesin translocation along DNA (Stigler et al., 2016) and that nucleosome removal promotes efficient loop extrusion in *Xenopus* egg extracts (Golfier et al., 2020). Moreover, numerous studies suggest that cohesin loading on chromosomes occurs at nucleosome-depleted regions (often associated with transcription start sites) and requires ATP-dependent nucleosome remodeling activities (Garcia-Luis et al., 2019; Golfier et al., 2020; Munoz et al., 2019). In addition, it has been suggested that cohesin translocation requires transcription-coupled nucleosome remodeling (D'Ambrosio et al., 2008; Dubey and Gartenberg, 2007; Glynn et al., 2004; Hu et al., 2011; Lengronne et al., 2004; Ocampo-Hafalla et al., 2016; Schmidt et al., 2009). However, some recent studies suggest the possibility that loop extrusion can proceed over nucleosomes, albeit at low nucleosome density (Golfier et al., 2020; Kim et al., 2019). If nucleosomes (or a subset of nucleosomes, if histone modifications have an impact) do serve as barriers to loop extrusion, then ATP-dependent nucleosome remodeling would be expected to play important roles in TAD formation. Our work suggests that the INO80 chromatin remodeler carries out an important role in driving chromatin mobility in a manner that appears independent of the impact of looping interactions on chromatin dynamics. However, this does not rule out collaboration of nucleosome remodelers on the act of loop extrusion, which remains an exciting avenue for further study.

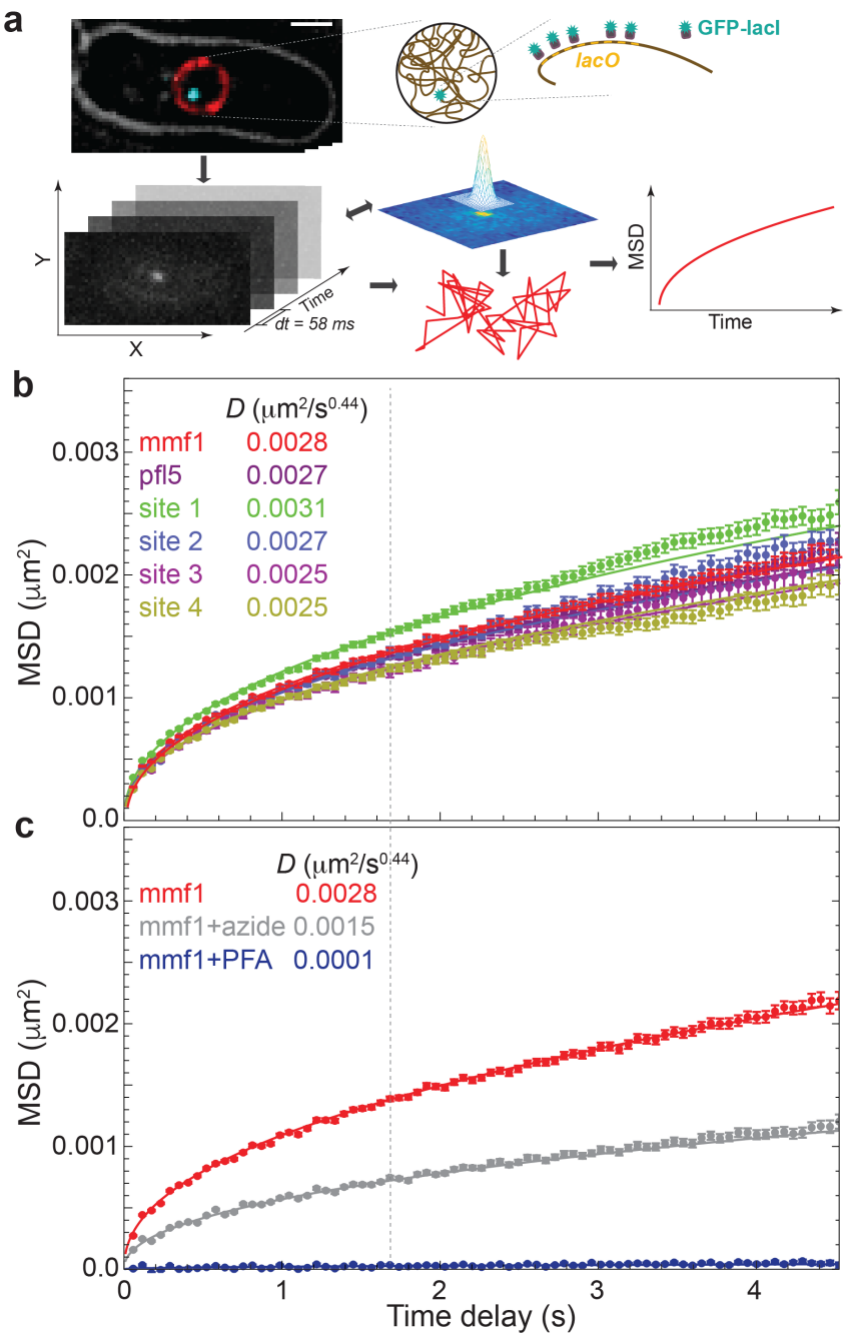

Fig. 1. DNA loci of individual cells are visualized and tracked over time to measure chromatin dynamics. (a) Cells labeled with a *lacO* array inserted adjacent to the gene of interest or at random are visualized using GFP-LacI fluorescence. DNA loci are tracked using a custom 2D single particle tracking algorithm (Bailey et al., 2021). (b) Chromatin diffusivity is nearly identical across six different genomic locations as shown by the mean squared displacement (MSD) of each genetic locus as a function of the time window of observation, along with its calculated diffusion coefficient, D. (c) Cells treated with sodium azide show attenuation of chromatin dynamics by depletion of ATP. For comparison, we imaged cells fixed with formaldehyde to assess the lower limit of movement detectable with our image acquisition and 2D particle tracking system. Error bars in (b) and (c) designate standard errors of the mean.

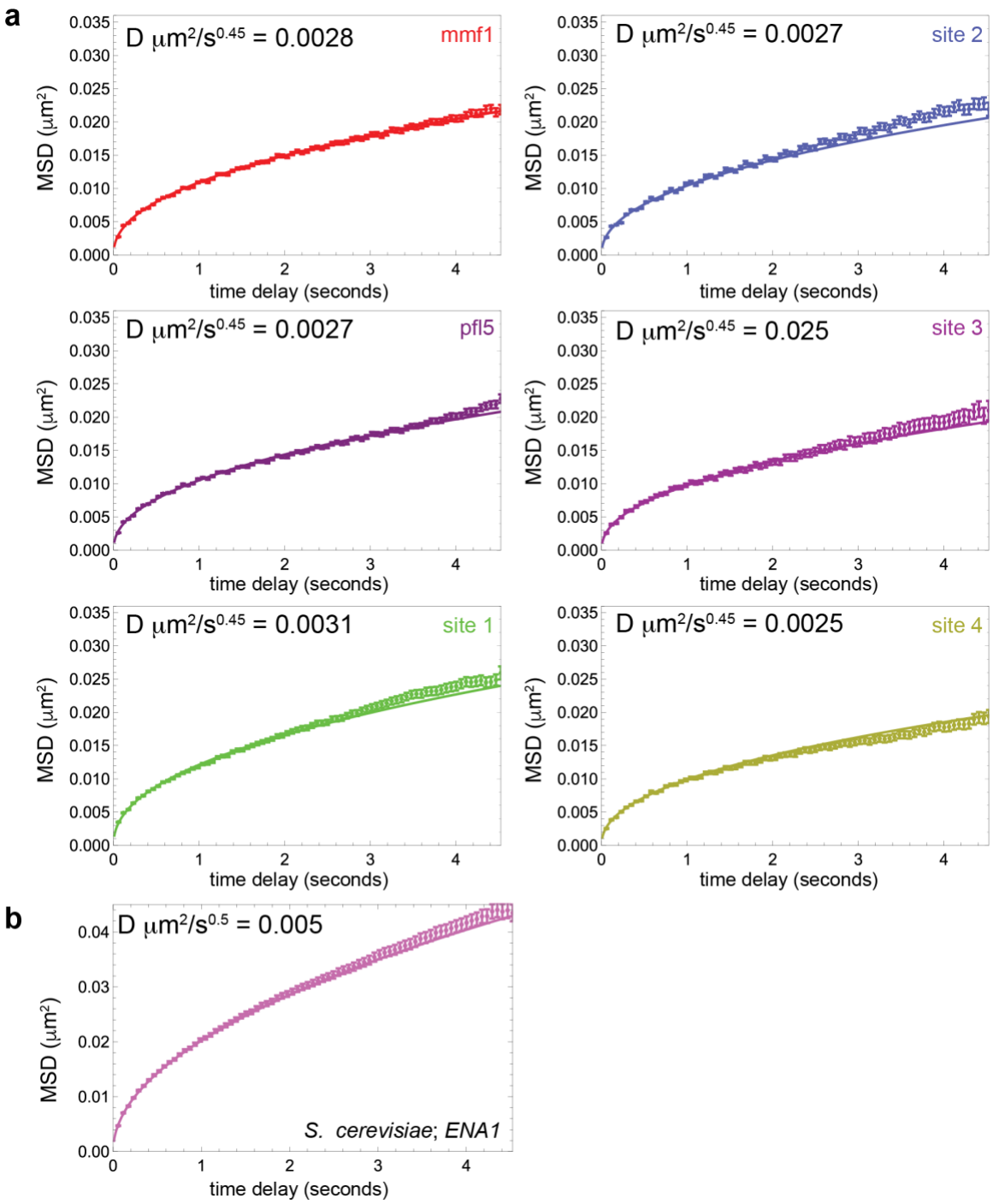

Fig. 1. – figure supplement 1. Individual MSD plots for fission yeast and budding yeast. (a) Chromatin diffusivity is nearly identical across six different genomic locations as shown by the mean squared displacement (MSD) of each genetic locus as a function of the time window of observation, along with its calculated diffusion coefficient, D. (b) For comparison to previous chromatin dynamics measurements, we performed our visualization/tracking/diffusive analysis regime on *S. cerevisiae* cells integrated with a *lacO* array at the *ENA1* locus, resulting in a comparable diffusion coefficient as reported elsewhere. Error bars indicate standard errors of the mean.

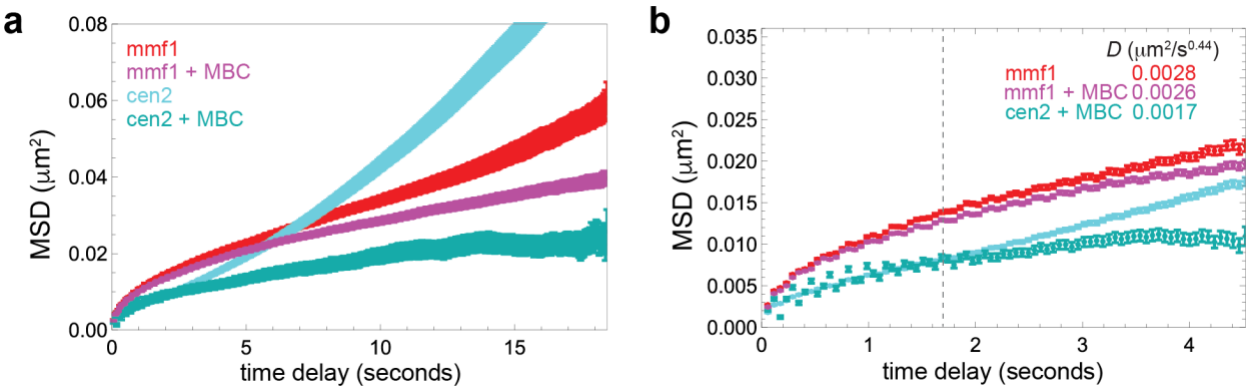

Fig. 2. Microtubule dynamics actively drive chromatin motion at the centromeres and, to a lesser extent, the chromosome arms in fission yeast. In *S. pombe*, large-scale chromatin dynamics are governed by movement of the spindle pole body through each centromere's attachment (Funabiki et al., 1993). (a) The centromeres (*cen2*) demonstrate actively driven motion at the tens of seconds time scale as revealed by MSD analysis. Upon addition of the microtubule-depolymerizing agent carbendazim (MBC), this mobility is greatly depressed. The effect of microtubule dynamics is far less prominent for a locus in the chromosome arm (*mmf1*). (b) On the seconds time scale, the mobility of *cen2* is far more constrained than the *mmf1* locus and microtubule dynamics play a more muted effect. Error bars indicate standard errors of the mean.

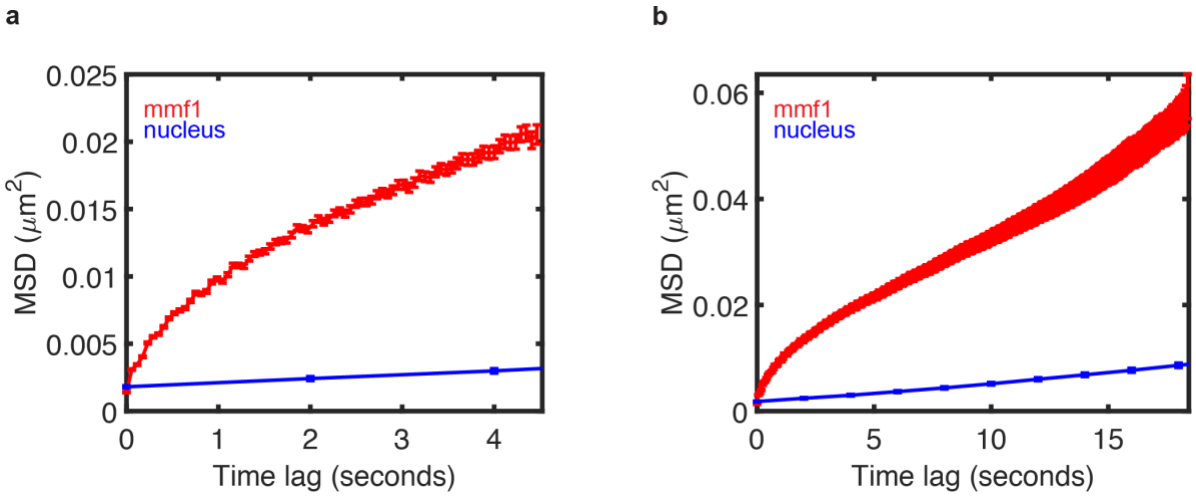

Fig. 2 – figure supplement 1. Microtubule-dependent chromatin mobility has only a minor contribution from rigid body motion of the nucleus. (a,b) Comparison of the MSD on the seconds time scale (a) and tens of seconds time scale (b) for a *lacO* array at *mmf1* (red) compared to the rigid body movement of the nucleus (blue) over the same time scale. *mmf1* data replotted from Fig. 2.

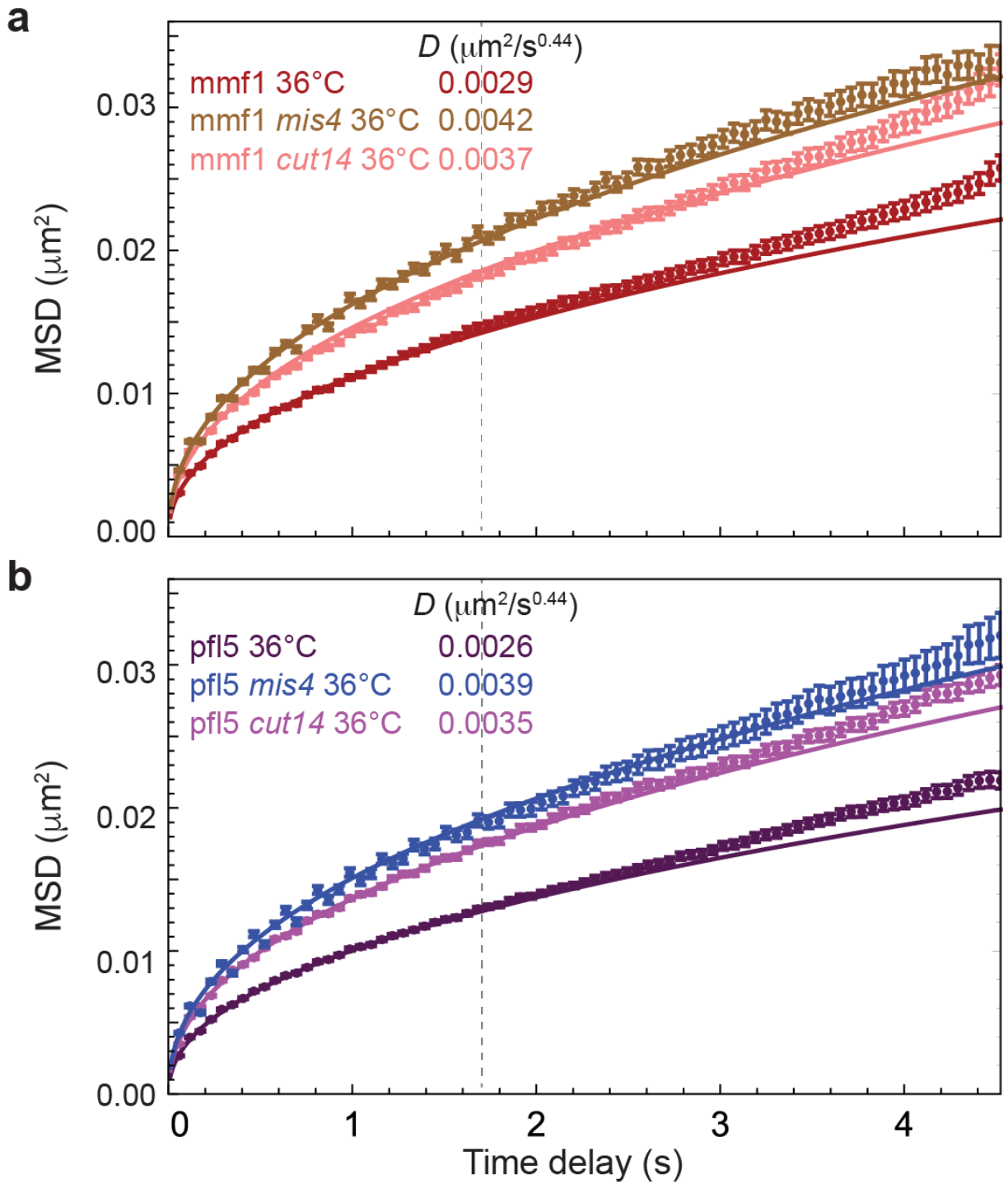

Fig. 3. Loss of cohesin or condensin activity increases chromatin mobility (a) Temperature-sensitive alleles of the cohesin-loading protein Mis4 and condensin complex subunit 2 (Cut14) imaged at the non-permissive temperature allow for inhibition of cohesin and condensin function, respectively, and show enhanced diffusivity at the *mmf1* locus. (b) The same enhancement of chromatin dynamics is observed at a separate genomic locus, *pfl5*. Error bars indicate standard errors of the mean.

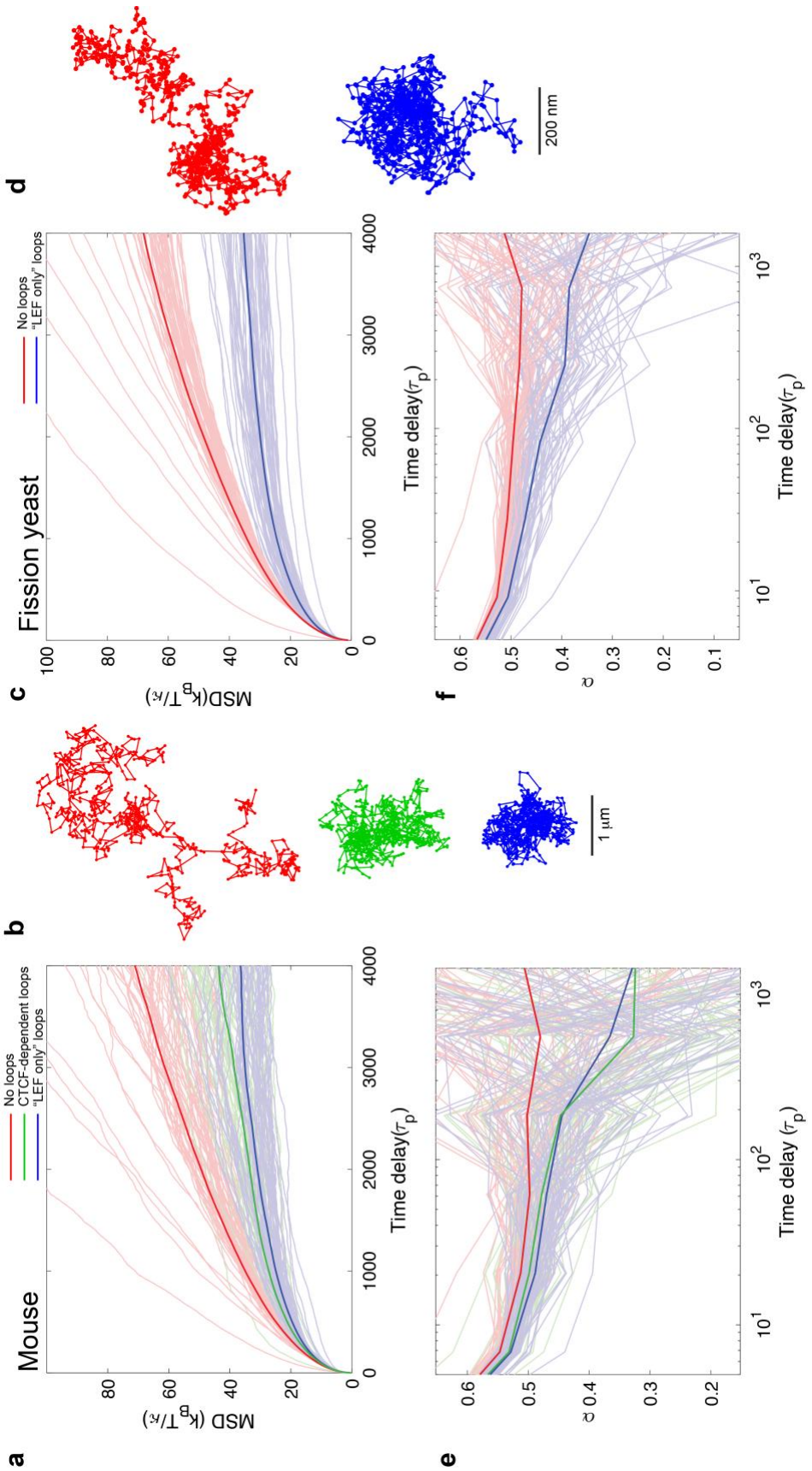
a
Mouse
No loops
CTCF-dependent loops
"LEF only" loops
MSD (k_BT/κ)
Time delay(τ_p)
b
1 μm
c
Fission yeast
No loops
"LEF only" loops
MSD(k_BT/κ)
Time delay(τ_p)
d
200 nm
e
α
Time delay (τ_p)
f
α
Time delay(τ_p)

Fig. 4. LEF activity constrains chromatin motion as revealed by Rouse-type polymer simulations. (a) The formation of time-dependent loops driven by loop extrusion according to the CTCF (green) or “LEF only” model lacking explicit boundaries (blue) applied to the mouse genome leads to decreased mean-squared displacements (MSD) compared to the polymer without loops (red). MSDs arise from a Rouse-model with beads of friction coefficient ζ, connected by springs of spring constant κ. (b) Examples of the instantaneous polymer configurations from the simulations. (c) The same analysis described in (a) but applied to the fission yeast genome for the “LEF only” model (blue) compared to the polymer without loops (red). (e) Examples of the instantaneous polymer configurations from fission yeast. (e) and (f) Effective exponent, α, versus time for the mouse (e) and yeast (f) models, respectively. In (a,b) and (e,f), thin lines correspond to individual beads, thick lines represent the average over all beads.

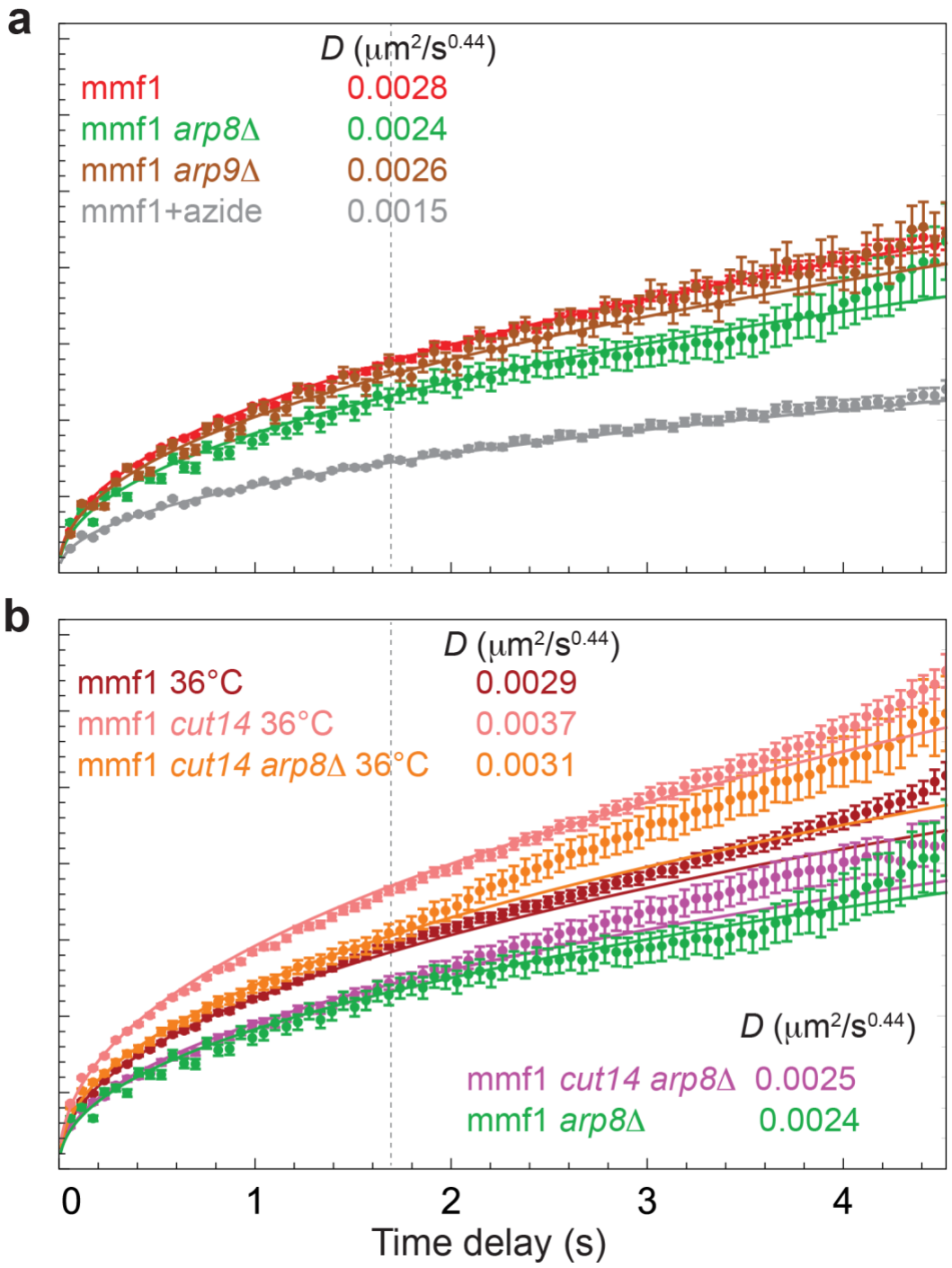

Fig. 5. Loss of the nucleosomal remodeling complex protein Arp8 decreases chromatin mobility likely through a mechanism distinct from loop extrusion. (a) Loss of Arp8, a component of the INO80 complex, reduces chromatin mobility by ~40%, while loss of Arp9, a component of both the SWR1 and RSC complexes, has minimal effect. For comparison, cells depleted of ATP (treated with sodium azide) are shown (replotted from Fig. 1c). (b) Loss of Arp8 dampens the elevated chromatin dynamics in the *cut14-208* background at the non-permissive temperature to a slightly less extent than in WT cells (a ~30% decrease) but remains much more diffusive than at the permissive temperature. Error bars indicate standard errors of the mean.

Materials and Methods:

Strain generation and culturing

All strains used in this study are listed in Table S3. *S. pombe* were grown, maintained, and crossed using standard procedures and media (Moreno et al., 1991). Gene replacements were made by exchanging open reading frames with various MX6-based drug resistance genes (Bähler et al., 1998; Hentges et al., 2005). Targeted *lacO* array insertions were generated using a modified two-step integration procedure that first creates a site-specific DNA double-strand break to increase targeting efficiency of the linearized plasmid pSR10_ura4_10.3kb (Leland and King, 2014); integration sites are listed in Table S3. Random *lacO* array insertions were generated by transformation of the GFP-LacI-expressing strain MKSP1120 with linearized plasmid pSR10_ura4_10.3kb followed by selection on plates lacking uracil as in (Leland and King, 2014). Strains that had successfully inserted *lacO* array were identified by fluorescence microscopy. The *S. cerevisiae* strains used in this study were constructed, grown and imaged as described in (Colombi et al., 2018).

Microscopy

Cells were grown in YE5S media (yeast extract plus five supplements; (5 g/L yeast extract (BD Bacto), and 0.25 g/L adenine, 0.25 g/L histidine, 0.25 g/L leucine, 0.25 g/L lysine, and 0.25 g/L uracil, (Sunrise Science Products)) at 30°C to log phase (OD600 0.5–0.8). For temperature-sensitive alleles, the cells were grown at 30°C then shifted for twenty minutes to the non-permissive temperature (36°C) prior to imaging. For pharmacological inhibition studies, cells were incubated at 30°C with sodium azide (0.02% w/v) or with 50 mg/ml MBC (methyl-2-benzimidazol-2-ylcarbamate) for 10 min prior to imaging. To fix cells, cells were incubated with 2% paraformaldehyde for 10 min and washed once with 2X PBS (phosphate-buffered saline).

For imaging, 1.4 µL of the concentrated cell suspension was transferred to a ~1 cm x 1 cm x 1 mm pad made of 1.4% agarose (Denville Scientific) in EMM5S media (Edinburgh minimal media plus five supplements 0.25 g/L adenine, 0.25 g/L histidine, 0.25 g/L leucine, 0.25 g/L lysine, and 0.25 g/L uracil (Sunrise Science Products)) on a microscope slide. The cell pad was covered with a #1.5 – 22 x 22 mm coverslip, and edges were sealed with VALAP (1:1:1 petroleum jelly, lanolin, and paraffin) to limit evaporation during imaging.

Fluorescence and bright field images were acquired on a DeltaVision widefield microscope (Applied Precision/GE) equipped with a temperature control chamber, 1.4 NA 100x objective (Olympus), solid-state-based illumination (Lumencor), and an Evolve 512 EMCCD camera (Photometrics). Fluorescence was excited at 488 nm and collected with emission filters between 500-550nm. Typically, 1000 images were continuously acquired with 10 ms exposure time and 58 ms per frame rate.

Loci tracking and trajectory analysis

The localization of each fluorescently-labeled chromatin focus was determined by applying a spatial bandpass filter to each raw image frame. Specifically, the centroid of each peak above a determined threshold value was calculated to obtain an approximate position. Then, the final localization was obtained by fitting a radially symmetric Gaussian function around each centroid position. These positions were then linked into time trajectories using the algorithm for single particle tracking introduced in (Crocker and Grier, 1996). Specifically, we did not allow gaps between frames, we set the maximum displacement between frames to 2 pixels (0.321 μm), and we set the minimum track length to be 300 frames, or 100 frames for experiments involving *arp8Δ*, *arp9Δ*, and *cut14-208/arp8Δ* genotypes or sodium azide treatment. The mean-square displacement (MSD) versus time delay for each time-lapse image series was calculated as follows. First, the trajectories were split into sub-trajectories of 29 steps (with duration ≈ 1.68 s). Then, individual displacements were averaged across all sub-trajectories and different time-lapse series for a given experiment. The calculated experimental MSDs were fit by the theoretical MSD for fractional Brownian motion (fBm) with static and dynamic localization errors taken into account, as described (Bailey et al., 2021):

$$M_n = \frac{4D(\Delta t)^{2+\alpha}\left(\left(n-\frac{\Delta t_E}{\Delta t}\right)^{2+\alpha} - 2n^{2+\alpha} + \left(n+\frac{\Delta t_E}{\Delta t}\right)^{2+\alpha}\right)}{(1+\alpha)(2+\alpha)\Delta t_E^2} - \frac{8D\Delta t_E^{\alpha}}{(1+\alpha)(2+\alpha)} + 2\sigma^2 \qquad \text{[Eq. 1]}$$

where D is an effective diffusivity, Δt_E = 10 ms is exposure time, Δt is the time step between frames, and α is an exponent ($\alpha < 1$ corresponds to sub-diffusive motion and $\alpha > 1$ to super-diffusive motion), n is the number of frames, and σ is the static localization error. Initial MSD fitting, in which D, α, and σ were varied, showed that the values of α grouped around a mean of 0.44 for most measured loci in unperturbed, wild type cells (Supplementary Information Table S1). In all subsequent analyses (see Figs. 1, 2b, 3, 5), α was fixed at $\alpha = 0.44$, while D and σ were varied, allowing us to directly compare values of D as a measure of locus mobility across different

experiments. Supplementary Information Table S1 contains all the fitting results.

Whole-nucleus motion tracking

To estimate the potential contribution of rigid body motion of the nucleus to chromatin dynamics, we measured the dynamics of nuclei in a strain expressing a fluorescently-tagged form of the nucleoporin, Cut11 (Cut11-mCherry). Single central plane fluorescent images were acquired every 2 seconds. First, approximate nuclei positions were detected using a custom-written routine in MATLAB. Next, each detected fluorescent image of the nuclear envelope rim was fitted (using custom-written routine in MATLAB) by a circle convolved with the point-spread function with the center position, circled radius, fluorescence amplitude and background as free parameters. Last, the position of each nuclear center was tracked by the same approach described used for the loci tracking and trajectory analysis.

Gillespie simulations

We carried out Gillespie-type simulations (Gillespie, 1977) of the chromatin loop configuration using two different models of loop formation and extrusion. First, we simulated a version of the model described in (Fudenberg et al., 2016). Subsequent to uniformly-distributed random binding, LEF translocation proceeds bidirectionally until either the LEF dissociates or a LEF anchor encounters another LEF or a boundary element (BE). LEFs cannot pass each other. However, BEs have a non-zero permeability, P, which is implemented as a multiplier to the LEF translocation rate at BEs, that is, $v_{BE} = Pv$, where v is the LEF translocation rate away from BEs and v_{BE} is the translocation rate at BEs. CTCF ChIP-seq data is used to determine the locations of boundary element (BEs), as well as their permeability, which is determined from the CTCF ChIP-seq signal, S, via a logistic function:

$$P = \frac{1}{1 + e^{(S/S_0 - \mu)}},$$

where S_0 is the maximum CTCF signal and μ is a scale parameter to be optimized. Second, since *S. pombe* lack CTCF, we also carried out simulations without any BEs, but that were otherwise the same. For each set of parameter values, we performed ten simulations, each comprising 1,000,000 time steps. Loop dynamics reached a steady state over about 15,000 steps as gauged by convergence of the chromatin backbone length to a more-or-less constant value. 6 Mb (300 kb) genomic regions for mouse (yeast) were divided into 10 kb (0.5 kb) bins

creating 600 sites that could be occupied by one side of a LEF. Our loop-extrusion simulation code is online at the github repository: https://github.com/nilesyan/LEF-Simulation.

Polymer simulations

Chromatin's polymer behavior was modeled as a Rouse (bead-spring) chain, in which each 10 kb (0.5 kb) region of the mouse (yeast) genome is represented as a bead that is connected to its nearest neighbors by springs of stiffness, κ, and experiences fluid friction with coefficient, ζ. To include loops, we augmented the model with additional springs (of the same spring constant) that connect non-adjacent beads, representing the base of a loop. For the simulations shown in Fig. 4, the characteristic polymer time, defined here as the inverse of the smallest Rouse-model eigenvalue, namely $\tau_P = \frac{\zeta}{4\kappa}$, was calculated on the basis of the parameters determined in (Arbona et al., 2017), assuming a LEF translocation velocity of 30 bp s^{-1}. However, the resultant MSDs are indistinguishable from those obtained for LEF velocities of 3 bp s^{-1} and 300 bp s^{-1}. The number, sizes, and locations of loops evolve according to our loop extrusion simulations. Since the additional springs lead to far-from-diagonal terms in the Rouse-model dynamical matrix, the matrix was diagonalized numerically to find the eigenmodes and corresponding beads-to-eigenmode transformations. Assuming equipartition with an effective temperature, these eigenmodes (and, through transformations, the corresponding bead positions) were then evolved using the exact simulation method of (Gillespie, 1996) until the loop configuration changed. This procedure was then repeated for each new loop configuration. Because this approach allows us to simulate polymer dynamics with arbitrary time steps in our simulations, we combined an equally-spaced time series (with time step shorter than the polymer time) with the exact times of loop extrusion events, ensuring an exact simulation in the presence of loop extrusion. Finally, mean MSDs were calculated by averaging MSDs of individual beads (Fig. 4).

Contributions

J.F.W. and I.S. generated all yeast strains and raw movies for analysis of chromatin mobility. M.P.B. designed, implemented and plotted all loci tracking and trajectory analysis. H.Y. and T.Y. designed and performed the Gillespie and polymer simulations with input from I.S. and S.G.J.M. M.C.K. and S.G.J.M. conceived of the project, coordinated the team strategy and provided experimental direction. The manuscript was written, edited and approved by all authors.

Acknowledgements

We thank Bryan Leland, Amanda Vines, Paolo Colombi, Dongxu Lin, Sara Siwiecki, and Ryan Brennan for generating strains used in this work. We also thank the Yeast Genome Resource Center at Osaka University and the many investigators who have deposited strains at this resource. This work was supported by an NSF EFRI CEE award EFMA-1830904 to S.G.J. Mochrie and M.C. King. M.P.B. was supported by NIH T32EB019941 and the NSF GRFP. H.Y. was support by the NSF Physics of Living Systems Student Research Network via PHYS 1522467.

Supplemental Table S1: MSD Fitting Results

Strain	fitted alpha	Confidence Interval on alpha fit	free sigma^2	CI on sigma^2	free D	CI on D	alpha set to 0.44	alpha = 0.44 sigma^2	CI on sigma^2	alpha = 0.44 D	CI on D
mmf1 WT	0.43	0.3695 - 0.4955	0.0031	0.0027 - 0.0035	0.0028	0.0025 - 0.0032	**0.44**	0.0031	0.0030 - 0.0032	0.0028	0.0027 - 0.0029
pfl5 WT	0.42	0.3613 - 0.4883	0.003	0.0026 - 0.0034	0.0028	0.0025 - 0.0031	**0.44**	0.0031	0.0030 - 0.0032	0.0027	0.0026 - 0.0028
site 1	0.53	0.4910 - 0.5776	0.0033	0.0031 - 0.0035	0.0027	0.0025 - 0.0029	**0.44**	0.0027	0.0026 - 0.0029	0.0031	0.0030 - 0.0031
site2	0.41	0.3092 - 0.5172	0.0032	0.0025 - 0.0039	0.0028	0.0023 - 0.0033	**0.44**	0.0034	0.0032 - 0.0036	0.0027	0.0026 - 0.0028
site 3	0.43	0.3662 - 0.4901	0.003	0.0026 - 0.0034	0.0026	0.0023 - 0.0028	**0.44**	0.0031	0.0029 - 0.0032	0.0025	0.0025 - 0.0026
site 4	0.41	0.3540 - 0.4641	0.0028	0.0024 - 0.0031	0.0027	0.0024 - 0.0030	**0.44**	0.0029	0.0028 - 0.0030	0.0025	0.0025 - 0.0026
mmf1 cut14 36C	0.54	0.5081 - 0.5764	0.0029	0.0027 - 0.0032	0.0032	0.0031 - 0.0034	**0.44**	0.0022	0.0021 - 0.0023	0.0037	0.0037 - 0.0038
mmf1 mis4 36C	0.47	0.3828 - 0.5503	0.003	0.0023 - 0.0038	0.004	0.0035 - 0.0045	**0.44**	0.0028	0.0026 - 0.0031	0.0042	0.0040 - 0.0043
pfl5 cut14 36C	0.43	0.3918 - 0.4750	0.0025	0.0022 - 0.0029	0.0035	0.0033 - 0.0038	**0.44**	0.0026	0.0025 - 0.0027	0.0035	0.0035 - 0.0036
pfl5 mis4 36C	0.44	0.3187 - 0.5572	0.003	0.0019 - 0.0040	0.0039	0.0031 - 0.0047	**0.44**	0.003	0.0027 - 0.0033	0.0039	0.0037 - 0.0041
mmf1 36C	0.48	0.4462 - 0.5170	0.0031	0.0029 - 0.0033	0.0027	0.0026 - 0.0028	**0.44**	0.0029	0.0028 - 0.0029	0.0029	0.0028 - 0.0029
pfl5 36C	0.45	0.4154 - 0.4839	0.0026	0.0024 - 0.0028	0.0025	0.0024 - 0.0027	**0.44**	0.0026	0.0025 - 0.0026	0.0026	0.0026 - 0.0027
mmf1 pfa	note: mostly flat MSD	0.0033	0.0029 - 0.0036	5.50E-05	-2.1e-4 - 3.3e-4	**0.44**	0.0033	0.0032 - 0.0034	0.00005	-3.4e-6 - 1.10 e-4	
mmf1 nan3	0.46	0.3384 - 0.5864	0.0029	0.0025 - 0.0033	0.0014	0.0011 - 0.0017	**0.44**	0.0028	0.0027 - 0.0029	0.0015	0.0014 - 0.0016
mmf1 MBC	0.42	0.3327 - 0.4717	0.0027	0.0023 - 0.0032	0.0028	0.0024 - 0.0032	**0.44**	0.0029	0.0028 - 0.0031	0.0026	0.0026 - 0.0027
arp8	0.68	0.4822 - 0.8815	0.004	0.0034 - 0.0046	0.0017	0.0014 - 0.0021	**0.44**	0.0031	0.0027 - 0.0034	0.0024	0.0022 - 0.0025
arp8 cut14 30C	0.54	0.4857 - 0.5969	0.003	0.0028 - 0.0033	0.0021	0.0020 - 0.0023	**0.44**	0.0026	0.0024 - 0.0027	0.0025	0.0024 - 0.0025
arp8 cut14 36C	0.68	0.6290 - 0.7331	0.0034	0.0032 - 0.0037	0.0023	0.0022 - 0.0024	**0.44**	0.0023	0.0020 - 0.0025	0.0031	0.0030 - 0.0032
arp9	0.44	0.2652 - 0.6106	0.0037	0.0027 - 0.0047	0.0026	0.0019 - 0.0034	**0.44**	0.0037	0.0034 - 0.0040	0.0026	0.0025 - 0.0028

ENA (cerev)	0.506	0.48 - 0.5326	0.0033	0.0031 0.0036	0.005	0.0048 - 0.0052				0.005	
cen2 + MBC	0.55	0.1309-0.9721	0.0042	0.0029-0.0054	0.0014	6.21e-4-0.0023	**0.44**	0.0038	0.0033-0.0043	0.0017	0.0014-0.0020

Supplemental Table S2 Rouse Simulation Parameters

	Mouse CTCF Model	**Mouse LEF Only Model**	***S. pombe* LEF Only Model**
LEF stepping rate (bp s^{-1})	30	30	600
LEF bind rate (s^{-1})	0.103	0.5	0.5
LEF unbind rate (s^{-1})	$1*10^{-4}$	$1.67*10^{-5}$	$3.16*10^{-5}$
CTCF scale parameter	23	N/A	N/A
Remodeler bind rate (s^{-1})	N/A	0.581	9.28
Number of LEFs	24	30	34
Polymer characteristic time (s)	26.3	26.3	0.0658

626 **Supplemental Table S3. Strains used in the study**

Strain	Relevant genotype	Description	Source
S. pombe			
Specific lacO *position*			
MKSP1642	*h+ leu1-32 ura4-D18 his7+:P_{Dis1}-gfp-lacI-NLS sad1::sad1-dsRed-leu+ cen2:ura4-lacO$_n$*	WT strain with *lacO* array integrated near *cen2* (Chr2 centromere) locus and with expression of LacI-GFP (with nucleus localization signal) under control of the constitutive promoter. *Fig. 2, Fig2-fig supp1*	*this study derived from* PX342 and PN10127
MKSP1661	*h+ leu1-32 ura4-D18 his7+:P_{Dis1}-gfp-lacI-NLS cut11::cut11-mCherry-natR pfl5: ura4-lacO$_n$*	WT strain with *lacO* array (5.6 kb) integrated near *pfl5* locus (at *ChrII: 4403547-4403553*). *Fig. 1b, 3b and Fig1-fig supp1a*.	[1]
MKSP1794	*leu1-32 ura4-D18 mis4::mis4-242^{ts} his7+:P_{Dis1}-gfp-lacI-NLS cut11::cut11-mCherry-natR pfl5:ura4-lacO$_n$*	Temperature-sensitive mutant of Mis4 cohesin loading factor with *lacO* array (5.6 kb) integrated near *pfl5* locus. *Fig. 3.*	*this study derived from* MY3655 and *MKSP1340*
MKSP2039	*h- leu1-32 ura4-D18 his7+:P_{Dis1}-gfp-lacI-NLS mmf1:ura4-lacO$_n$*	WT strain with *lacO* array (10.3 kb) integrated near *mmf1* locus (at *ChrII:3442981*). *Fig. 1b-c, 2, 3a, 5, Fig1-fig supp1, Fig2-fig supp1.*	*this study derived from MKSP1381*
MKSP2583	*h- leu1-32 ura4-D18 arp8::hygR his7+:P_{Dis1}-gfp-lacI-NLS mmf1:ura4-lacO$_n$ urg1:: loxP-kanR-loxM3*	*arp8* (INO80 complex subunit) deletion mutant with *lacO* array (10.3 kb) integrated near *mmf1* locus. *Fig. 5.*	*this study derived from* MKSP2190
MKSP2693	*leu1-32 ura4-D18 cut14::cut14-208^{ts} his7+:P_{Dis1}-gfp-lacI-NLS pfl5:ura4-lacO$_n$*	Temperature-sensitive mutant of Cut14 condensin subunit with *lacO* array (5.6 kb) integrated near *pfl5* locus. *Fig. 3b.*	*this study derived from* MY1983
MKSP2760	*leu1-32 ura4-D18 cut14::cut14-208^{ts} his7+:P_{Dis1}-gfp-lacI-NLS mmf1:ura4-lacO*	Temperature-sensitive mutant of Cut14 condensin subunit with *lacO* array (10.3 kb) integrated near *mmf1* locus. *Fig. 3a*	*this study derived from* MY1997
MKSP2801	*leu1-32 ura4-D18 mis4::mis4-242^{ts} his7+:P_{Dis1}-gfp-lacI-NLS cut11::cut11-mCherry-natR mmf1:ura4-lacO$_n$*	Temperature-sensitive mutant of Mis4 cohesin loading factor with *lacO* array (10.3 kb) integrated near *mmf1* locus. *Fig. 3a.*	*this study derived from* MY3655 and *MKSP1340*
MKSP3021	*leu1-32 ura4-D18 arp9::kanR his7+:P_{Dis1}-gfp-lacI-NLS mmf1:ura4-lacO$_n$*	*arp9* (SWI/RSC complexes subunit) deletion with *lacO* array (10.3 kb) integrated near *mmf1* locus. *Fig. 5a.*	*this study derived from* MKSP2352
MKSP3053	*leu1-32 ura4-D18 arp8::kanR cut14::cut14-208^{ts} his7+:P_{Dis1}-gfp-lacI-NLS mmf1:ura4-lacO$_n$*	Double mutant with *arp8* deletion and temperature-sensitive mutant of Cut14 condensin subunit with *lacO* array (10.3 kb) integrated near *mmf1* locus. *Fig. 5b.*	*this study derived from* MKSP2187
Random lacO *position*			
MKSP3117	*h+ leu1-32 ura4-D18 his7+:P_{Dis1}-gfp-lacI-NLS random locus:ura4-lacO$_n$*	WT strain with *lacO* array (10.3 kb) integrated at random locus of the genome (noted as “site1”), and with LacI-GFP (with nucleus localization signal) under control of the constitutive promoter. *Fig. 1b* and *Fig1-fig supp1a.*	*derived from* MKSP1120
MKSP3118	*h+ leu1-32 ura4-D18 his7+:P_{Dis1}-gfp-lacI-NLS random locus:ura4-lacO$_n$*	Same as MKSP3117 but with a different random *lacO* array position (noted as “site2”). *Fig. 1b* and *Fig1-fig supp1a.*	*derived from* MKSP1120

MKSP3119	*h+ leu1-32 ura4-D18 his7+:P_{Dis1}-gfp-lacI-NLS random locus:ura4-lacO$_n$*	Same as MKSP3117 but with a different random *lacO* array position (noted as "site3"). *Fig. 1b* and *Fig1-fig supp1a.*	*derived from* MKSP1120
MKSP3123	*h+ leu1-32 ura4-D18 his7+:P_{Dis1}-gfp-lacI-NLS random locus:ura4-lacO$_n$*	Same as MKSP3117 but with a different random *lacO* array position (noted as "site4"). *Fig. 1b* and *Fig1-fig supp1a.*	*derived from* MKSP1120
Labeled nuclear envelope strain			
MKSP3140	*h+ leu1-32 ura4-D18 his7+:P_{Dis1}-gfp-lacI-NLS cut11::cut11-mCherry-natR isd90: ura4-lacO$_n$*	WT strain with *lacO* array (10 kb) integrated near *isd90* locus (at *ChrII: 1950422*). *Fig2-fig supp1*.	
Auxiliary strains			
AW563	*h− leu1-32 urg1:loxP-kanR-loxM3$_6$*	WT strain with recombination-mediated cassette exchange system (*RMCE$_{kanMX6}$*).	[2]
JM210 FN198 MKSP1116	*h- leu1-32 ura4-D18 ade- cut11::cut11-mCherry-natMX6*	WT strain with Cut11-mCherry (a nuclear envelope marker) expression controlled by the native promoter.	*Nurse lab*
MKSP1120	*h+ leu1-32 ura4-D18 his7+:P_{Dis1}-gfp-lacI-NLS*	WT strain with LacI-GFP (with nucleus localization signal) under control of the constitutive promoter. Used to generate random *lacO* array integrations.	
MKSP1340	*h- leu1-32 ura4-D18 his7+:P_{Dis1}-gfp-lacI-NLS cut11::cut11-mCherry-natR mmf1:ura4-lacO$_n$ ChrII:3442981::ura4-lacO$_n$*	WT strain with *lacO* array (10.3 kb) integrated near *mmf1* locus and with LacI-GFP (with nucleus localization signal) under control of the constitutive promoter	*this study similar to* MKSP1381
MKSP1381	*h- leu1-32 ura4-D18 his7+:P_{Dis1}-gfp-lacI-NLS ChrII:3442981::ura4-10.3kbLacO ChrII:3446249::HOcs-hphMX6 cut11::cut11-mCherry-natMX6*	Original *lacO* array (10.3 kb) integration near *mmf1* locus. Used to generate all other *mmf1-lacO$_n$* strains in this study	[3]
MKSP1128	*h- leu1-32 ura4-D18 his7+:P_{Dis1}-gfp-lacI-NLS cut11::cut11-mCherry-natMX6*	WT strain with Cut11-mCherry (a nuclear envelope marker) expression controlled by the native promoter and with LacI-GFP (with nucleus localization signal) under control of the constitutive promoter.	
MKSP2187	*h- leu1-32 ura4-D18 arp8::kanR*	*arp8* deletion.	*this study*
MKSP2190	*h- leu1-32 ura4-D18 arp8::hygR*	*arp8* deletion.	*this study*
MKSP2352	*h- leu1-32 ura4-D18 arp9::kanR*	*arp9* deletion.	*this study*
MY1983	*h- ura4 cut14::cut14-208^{ts}*	Strain encoding for the temperature sensitive allele of *cut14*.	*YGRC* FY9883
MY1997	*h+ cut14::cut14-208^{ts}*	Strain encoding for the temperature sensitive allele of *cut14*.	*YGRC* FY9897
MY3655	*h- leu1-32 mis4::mis4-242^{ts}*	Strain encoding for the temperature sensitive allele of *mis4*.	*YGRC* FY111578
PN10127	*h- sad1::sad1-dsRed-leu+*	WT strain with Sad1-dsRed (a spindle pole body marker) expression controlled by the native promoter.	
PX342	*h+ leu1-32 ade6-M216 bub1::ura4 cen2-lacO$_n$*	Strain with *cen2* locus (centromere of ChrII) containing *lacO* array insertion.	*YGRC* FY13812 [4]
S. cerevisiae			
PCCPL645	*W303 LacI-GFP::HIS*	W303 strain with *LacI-GFP* (with nucleus localization signal) under control of the constitutive promoter.	[5]

PCCPL835	*W303 LacI-GFP::HIS ENA-lacO$_n$::TRP1*	W303 strain with *lacO* array integrated near *ENA* locus and with *LacI-GFP* (with nucleus localization signal) under control of the constitutive promoter.	*this study derived from PCCPL 645 as described* [5] and [6]

References:

1. Zhao Y., Schreiner S.M., Koo P.K., Colombi P., King M.C., Mochrie S.G. (2016) Improved Determination of Subnuclear Position Enabled by Three-Dimensional Membrane Reconstruction. ***Biophys. J.*** 111, 19-24.

2. Watson A.T., Werler P., Carr A.M. (2011) Regulation of gene expression at the fission yeast Schizosaccharomyces pombe urg1 locus. **Gene** 484, 75-85.

3. Leland B.A., Chen A.C., Zhao A.Y., Wharton R.C., King M.C. (2018) Rev7 and 53BP1/Crb2 prevent RecQ helicase-dependent hyper-resection of DNA double-strand breaks. ***eLife*** 7, e33402.

4. Hauf S., Biswas A., Langegger M., Kawashima S.A., Tsukahara T, Watanabe Y. (2007) Aurora controls sister kinetochore mono-orientation and homolog bi-orientation in meiosis-I. ***EMBO J.*** 26, 4475-86.

5. Colombi P., King D.E., Williams J.F., Lusk C.L., King M.C. (2018) LEM domain proteins control the efficiency of adaptation through copy number variation. ***Bioarxiv*** 451583, https://www.biorxiv.org/content/biorxiv/early/2018/10/24/451583.full.pdf

6. Murray J., Watson A., Carr A. (2016) *Identifying products of recombinase-mediated cassette exchange (RMCE) in Schizosaccharomyces pombe.* **Cold Spring Harbor Protocols**, 2016 (5)

References

Alipour, E., and J.F. Marko. 2012. Self-organization of domain structures by DNA-loop-extruding enzymes. *Nucleic Acids Res*. 40:11202-12.10.1093/nar/gks925

Arbona, J.M., S. Herbert, E. Fabre, and C. Zimmer. 2017. Inferring the physical properties of yeast chromatin through Bayesian analysis of whole nucleus simulations. *Genome Biol*. 18:81.10.1186/s13059-017-1199-x

Bähler, J., J.Q. Wu, M.S. Longtine, N.G. Shah, A. McKenzie, A.B. Steever, A. Wach, P. Philippsen, and J.R. Pringle. 1998. Heterologous modules for efficient and versatile PCR-based gene targeting in Schizosaccharomyces pombe. *Yeast (Chichester, England)*. 14:943-951.10.1002/(SICI)1097-0061(199807)14:10<943::AID-YEA292>3.0.CO;2-Y

Bailey, M.L.P., H. Yan, I. Surovtsev, J.F. Williams, M.C. King, and S.G.J. Mochrie. 2021. Covariance distributions in single particle tracking. *Physical Review E*. 103:032405.10.1103/PhysRevE.103.032405

Banigan, E.J., and L.A. Mirny. 2020. Loop extrusion: theory meets single-molecule experiments. *Curr Opin Cell Biol*. 64:124-138.10.1016/j.ceb.2020.04.011

Banigan, E.J., A.A. van den Berg, H.B. Brandão, J.F. Marko, and L.A. Mirny. 2020. Chromosome organization by one-sided and two-sided loop extrusion. *Elife*. 9.10.7554/eLife.53558

Bintu, B., L.J. Mateo, J.H. Su, N.A. Sinnott-Armstrong, M. Parker, S. Kinrot, K. Yamaya, A.N. Boettiger, and X. Zhuang. 2018. Super-resolution chromatin tracing reveals domains and cooperative interactions in single cells. *Science*. 362.10.1126/science.aau1783

Caridi, C.P., C. D'Agostino, T. Ryu, G. Zapotoczny, L. Delabaere, X. Li, V.Y. Khodaverdian, N. Amaral, E. Lin, A.R. Rau, and I. Chiolo. 2018. Nuclear F-actin and myosins drive relocalization of heterochromatic breaks. *Nature*. 559:54-60.10.1038/s41586-018-0242-8

Cheblal, A., K. Challa, A. Seeber, K. Shimada, H. Yoshida, H.C. Ferreira, A. Amitai, and S.M. Gasser. 2020. DNA Damage-Induced Nucleosome Depletion Enhances Homology Search Independently of Local Break Movement. *Mol Cell*. 80:311-326.e4.10.1016/j.molcel.2020.09.002

Chuang, C.H., A.E. Carpenter, B. Fuchsova, T. Johnson, P. de Lanerolle, and A.S. Belmont. 2006. Long-range directional movement of an interphase chromosome site. *Curr Biol*. 16:825-31.10.1016/j.cub.2006.03.059

Colombi, P., D.E. King, J.F. Williams, C.P. Lusk, and M.C. King. 2018. LEM domain proteins control the efficiency of adaptation through copy number variation. *bioRxiv*:451583.10.1101/451583

Crocker, J.C., and D.G. Grier. 1996. Methods of Digital Video Microscopy for Colloidal Studies. *Journal of Colloid and Interface Science*. 179:298-310.https://doi.org/10.1006/jcis.1996.0217

D'Ambrosio, C., C.K. Schmidt, Y. Katou, G. Kelly, T. Itoh, K. Shirahige, and F. Uhlmann. 2008. Identification of cis-acting sites for condensin loading onto budding yeast chromosomes. *Genes Dev*. 22:2215-27.10.1101/gad.1675708

Davidson, I.F., B. Bauer, D. Goetz, W. Tang, G. Wutz, and J.M. Peters. 2019. DNA loop extrusion by human cohesin. *Science*. 366:1338-1345.10.1126/science.aaz3418

Dekker, J. 2014. Two ways to fold the genome during the cell cycle: insights obtained with chromosome conformation capture. *Epigenetics Chromatin*. 7:25.10.1186/1756-8935-7-25

Dixon, J.R., D.U. Gorkin, and B. Ren. 2016. Chromatin Domains: The Unit of Chromosome Organization. *Mol Cell*. 62:668-80.10.1016/j.molcel.2016.05.018

Dixon, J.R., S. Selvaraj, F. Yue, A. Kim, Y. Li, Y. Shen, M. Hu, J.S. Liu, and B. Ren. 2012. Topological domains in mammalian genomes identified by analysis of chromatin interactions. *Nature*. 485:376-80.10.1038/nature11082

Doi, M., and S.F. Edwards. 1986. The theory of polymer dynamics. Oxford University Press, New York.

Dubey, R.N., and M.R. Gartenberg. 2007. A tDNA establishes cohesion of a neighboring silent chromatin domain. *Genes Dev*. 21:2150-60.10.1101/gad.1583807

Falk, M., Y. Feodorova, N. Naumova, M. Imakaev, B.R. Lajoie, H. Leonhardt, B. Joffe, J. Dekker, G. Fudenberg, I. Solovei, and L.A. Mirny. 2019. Heterochromatin drives compartmentalization of inverted and conventional nuclei. *Nature*. 570:395-399.10.1038/s41586-019-1275-3

Flavahan, W.A., Y. Drier, B.B. Liau, S.M. Gillespie, A.S. Venteicher, A.O. Stemmer-Rachamimov, M.L. Suva, and B.E. Bernstein. 2016. Insulator dysfunction and oncogene activation in IDH mutant gliomas. *Nature*. 529:110-4.10.1038/nature16490

Fudenberg, G., M. Imakaev, C. Lu, A. Goloborodko, N. Abdennur, and L.A. Mirny. 2016. Formation of Chromosomal Domains by Loop Extrusion. *Cell Rep*. 15:2038-49.10.1016/j.celrep.2016.04.085

Funabiki, H., I. Hagan, S. Uzawa, and M. Yanagida. 1993. Cell cycle-dependent specific positioning and clustering of centromeres and telomeres in fission yeast. *J Cell Biol*. 121:961-76.10.1083/jcb.121.5.961

Ganji, M., I.A. Shaltiel, S. Bisht, E. Kim, A. Kalichava, C.H. Haering, and C. Dekker. 2018. Real-time imaging of DNA loop extrusion by condensin. *Science*. 360:102-105.10.1126/science.aar7831

Garcia-Luis, J., L. Lazar-Stefanita, P. Gutierrez-Escribano, A. Thierry, A. Cournac, A. Garcia, S. Gonzalez, M. Sanchez, A. Jarmuz, A. Montoya, M. Dore, H. Kramer, M.M. Karimi, F. Antequera, R. Koszul, and L. Aragon. 2019. FACT mediates cohesin function on chromatin. *Nat Struct Mol Biol*. 26:970-979.10.1038/s41594-019-0307-x

Gassler, J., H.B. Brandao, M. Imakaev, I.M. Flyamer, S. Ladstatter, W.A. Bickmore, J.M. Peters, L.A. Mirny, and K. Tachibana. 2017. A mechanism of cohesin-dependent loop extrusion organizes zygotic genome architecture. *EMBO J*. 36:3600-3618.10.15252/embj.201798083

Gillespie, D.T. 1977. Exact stochastic simulation of coupled chemical reactions. *The Journal of Physical Chemistry*. 81:2340-2361.10.1021/j100540a008

Gillespie, D.T. 1996. The mathematics of Brownian motion and Johnson noise. *American Journal of Physics*. 64:225-240.10.1119/1.18210

Glynn, E.F., P.C. Megee, H.G. Yu, C. Mistrot, E. Unal, D.E. Koshland, J.L. DeRisi, and J.L. Gerton. 2004. Genome-wide mapping of the cohesin complex in the yeast Saccharomyces cerevisiae. *PLoS Biol*. 2:E259.10.1371/journal.pbio.0020259

Golfier, S., T. Quail, H. Kimura, and J. Brugués. 2020. Cohesin and condensin extrude DNA loops in a cell cycle-dependent manner. *Elife*. 9.10.7554/eLife.53885

Gu, B., T. Swigut, A. Spencley, M.R. Bauer, M. Chung, T. Meyer, and J. Wysocka. 2018. Transcription-coupled changes in nuclear mobility of mammalian cis-regulatory elements. *Science*. 359:1050-1055.10.1126/science.aao3136

Haarhuis, J.H.I., R.H. van der Weide, V.A. Blomen, J.O. Yanez-Cuna, M. Amendola, M.S. van Ruiten, P.H.L. Krijger, H. Teunissen, R.H. Medema, B. van Steensel, T.R. Brummelkamp, E. de Wit, and B.D. Rowland. 2017. The Cohesin Release Factor WAPL Restricts Chromatin Loop Extension. *Cell*. 169:693-707 e14.10.1016/j.cell.2017.04.013

Haering, C.H., A.M. Farcas, P. Arumugam, J. Metson, and K. Nasmyth. 2008. The cohesin ring concatenates sister DNA molecules. *Nature*. 454:297-301.10.1038/nature07098

Hauer, M.H., A. Seeber, V. Singh, R. Thierry, R. Sack, A. Amitai, M. Kryzhanovska, J. Eglinger, D. Holcman, T. Owen-Hughes, and S.M. Gasser. 2017. Histone degradation in response

to DNA damage enhances chromatin dynamics and recombination rates. *Nat Struct Mol Biol*. 24:99-107.10.1038/nsmb.3347

Hentges, P., B. Van Driessche, L. Tafforeau, J. Vandenhaute, and A.M. Carr. 2005. Three novel antibiotic marker cassettes for gene disruption and marker switching in Schizosaccharomyces pombe. *Yeast*. 22:1013-9.10.1002/yea.1291

Heun, P., T. Laroche, M.K. Raghuraman, and S.M. Gasser. 2001. The positioning and dynamics of origins of replication in the budding yeast nucleus. *J Cell Biol*. 152:385-400.10.1083/jcb.152.2.385

Hu, B., T. Itoh, A. Mishra, Y. Katoh, K.L. Chan, W. Upcher, C. Godlee, M.B. Roig, K. Shirahige, and K. Nasmyth. 2011. ATP hydrolysis is required for relocating cohesin from sites occupied by its Scc2/4 loading complex. *Curr Biol*. 21:12-24.10.1016/j.cub.2010.12.004

Ibrahim, D.M., and S. Mundlos. 2020. The role of 3D chromatin domains in gene regulation: a multi-facetted view on genome organization. *Curr Opin Genet Dev*. 61:1-8.10.1016/j.gde.2020.02.015

Joyner, R.P., J.H. Tang, J. Helenius, E. Dultz, C. Brune, L.J. Holt, S. Huet, D.J. Müller, and K. Weis. 2016. A glucose-starvation response regulates the diffusion of macromolecules. *Elife*. 5.10.7554/eLife.09376

Kakui, Y., C. Barrington, D.J. Barry, T. Gerguri, X. Fu, P.A. Bates, B.S. Khatri, and F. Uhlmann. 2020. Fission yeast condensin contributes to interphase chromatin organization and prevents transcription-coupled DNA damage. *Genome Biol*. 21:272.10.1186/s13059-020-02183-0

Kim, Y., Z. Shi, H. Zhang, I.J. Finkelstein, and H. Yu. 2019. Human cohesin compacts DNA by loop extrusion. *Science*. 366:1345-1349.10.1126/science.aaz4475

Lawrimore, C.J., J. Lawrimore, Y. He, S. Chavez, and K. Bloom. 2020. Polymer perspective of genome mobilization. *Mutat Res*. 821:111706.10.1016/j.mrfmmm.2020.111706

Leland, B.A., and M.C. King. 2014. Using LacO arrays to monitor DNA double-strand break dynamics in live Schizosaccharomyces pombe cells. *Methods Mol Biol*. 1176:127-41.10.1007/978-1-4939-0992-6_11

Lengronne, A., Y. Katou, S. Mori, S. Yokobayashi, G.P. Kelly, T. Itoh, Y. Watanabe, K. Shirahige, and F. Uhlmann. 2004. Cohesin relocation from sites of chromosomal loading to places of convergent transcription. *Nature*. 430:573-8.10.1038/nature02742

Lottersberger, F., R.A. Karssemeijer, N. Dimitrova, and T. de Lange. 2015. 53BP1 and the LINC Complex Promote Microtubule-Dependent DSB Mobility and DNA Repair. *Cell*. 163:880-93.10.1016/j.cell.2015.09.057

Lupianez, D.G., K. Kraft, V. Heinrich, P. Krawitz, F. Brancati, E. Klopocki, D. Horn, H. Kayserili, J.M. Opitz, R. Laxova, F. Santos-Simarro, B. Gilbert-Dussardier, L. Wittler, M. Borschiwer, S.A. Haas, M. Osterwalder, M. Franke, B. Timmermann, J. Hecht, M. Spielmann, A. Visel, and S. Mundlos. 2015. Disruptions of topological chromatin domains cause pathogenic rewiring of gene-enhancer interactions. *Cell*. 161:1012-1025.10.1016/j.cell.2015.04.004

Marshall, W.F., A. Straight, J.F. Marko, J. Swedlow, A. Dernburg, A. Belmont, A.W. Murray, D.A. Agard, and J.W. Sedat. 1997. Interphase chromosomes undergo constrained diffusional motion in living cells. *Curr Biol*. 7:930-9.10.1016/s0960-9822(06)00412-x

Miné-Hattab, J., and R. Rothstein. 2013. DNA in motion during double-strand break repair. *Trends Cell Biol*. 23:529-36.10.1016/j.tcb.2013.05.006

Mizuguchi, T., G. Fudenberg, S. Mehta, J.M. Belton, N. Taneja, H.D. Folco, P. FitzGerald, J. Dekker, L. Mirny, J. Barrowman, and S.I. Grewal. 2014. Cohesin-dependent globules and heterochromatin shape 3D genome architecture in S. pombe. *Nature*. 516:432-5.10.1038/nature13833

Moreno, S., A. Klar, and P. Nurse. 1991. Molecular genetic analysis of fission yeast Schizosaccharomyces pombe. *Methods Enzymol*. 194:795-823.10.1016/0076-6879(91)94059-l

Munoz, S., M. Minamino, C.S. Casas-Delucchi, H. Patel, and F. Uhlmann. 2019. A Role for Chromatin Remodeling in Cohesin Loading onto Chromosomes. *Mol Cell*. 74:664-673 e5.10.1016/j.molcel.2019.02.027

Neumann, F.R., V. Dion, L.R. Gehlen, M. Tsai-Pflugfelder, R. Schmid, A. Taddei, and S.M. Gasser. 2012. Targeted INO80 enhances subnuclear chromatin movement and ectopic homologous recombination. *Genes Dev*. 26:369-83.10.1101/gad.176156.111

Nora, E.P., B.R. Lajoie, E.G. Schulz, L. Giorgetti, I. Okamoto, N. Servant, T. Piolot, N.L. van Berkum, J. Meisig, J. Sedat, J. Gribnau, E. Barillot, N. Bluthgen, J. Dekker, and E. Heard. 2012. Spatial partitioning of the regulatory landscape of the X-inactivation centre. *Nature*. 485:381-5.10.1038/nature11049

Nuebler, J., G. Fudenberg, M. Imakaev, N. Abdennur, and L.A. Mirny. 2018. Chromatin organization by an interplay of loop extrusion and compartmental segregation. *Proc Natl Acad Sci U S A*. 115:E6697-E6706.10.1073/pnas.1717730115

Ocampo-Hafalla, M., S. Munoz, C.P. Samora, and F. Uhlmann. 2016. Evidence for cohesin sliding along budding yeast chromosomes. *Open Biol*. 6.10.1098/rsob.150178

Oshidari, R., J. Strecker, D.K.C. Chung, K.J. Abraham, J.N.Y. Chan, C.J. Damaren, and K. Mekhail. 2018. Nuclear microtubule filaments mediate non-linear directional motion of chromatin and promote DNA repair. *Nat Commun*. 9:2567.10.1038/s41467-018-05009-7

Parelho, V., S. Hadjur, M. Spivakov, M. Leleu, S. Sauer, H.C. Gregson, A. Jarmuz, C. Canzonetta, Z. Webster, T. Nesterova, B.S. Cobb, K. Yokomori, N. Dillon, L. Aragon, A.G. Fisher, and M. Merkenschlager. 2008. Cohesins functionally associate with CTCF on mammalian chromosome arms. *Cell*. 132:422-33.10.1016/j.cell.2008.01.011

Rao, S.S.P., S.C. Huang, B. Glenn St Hilaire, J.M. Engreitz, E.M. Perez, K.R. Kieffer-Kwon, A.L. Sanborn, S.E. Johnstone, G.D. Bascom, I.D. Bochkov, X. Huang, M.S. Shamim, J. Shin, D. Turner, Z. Ye, A.D. Omer, J.T. Robinson, T. Schlick, B.E. Bernstein, R. Casellas, E.S. Lander, and E.L. Aiden. 2017. Cohesin Loss Eliminates All Loop Domains. *Cell*. 171:305-320 e24.10.1016/j.cell.2017.09.026

Schmidt, C.K., N. Brookes, and F. Uhlmann. 2009. Conserved features of cohesin binding along fission yeast chromosomes. *Genome Biol*. 10:R52.10.1186/gb-2009-10-5-r52

Schrank, B.R., T. Aparicio, Y. Li, W. Chang, B.T. Chait, G.G. Gundersen, M.E. Gottesman, and J. Gautier. 2018. Nuclear ARP2/3 drives DNA break clustering for homology-directed repair. *Nature*. 559:61-66.10.1038/s41586-018-0237-5

Seeber, A., V. Dion, and S.M. Gasser. 2013. Checkpoint kinases and the INO80 nucleosome remodeling complex enhance global chromatin mobility in response to DNA damage. *Genes Dev*. 27:1999-2008.10.1101/gad.222992.113

Sexton, T., E. Yaffe, E. Kenigsberg, F. Bantignies, B. Leblanc, M. Hoichman, H. Parrinello, A. Tanay, and G. Cavalli. 2012. Three-dimensional folding and functional organization principles of the Drosophila genome. *Cell*. 148:458-72.10.1016/j.cell.2012.01.010

Shen, Y., F. Yue, D.F. McCleary, Z. Ye, L. Edsall, S. Kuan, U. Wagner, J. Dixon, L. Lee, V.V. Lobanenkov, and B. Ren. 2012. A map of the cis-regulatory sequences in the mouse genome. *Nature*. 488:116-20.10.1038/nature11243

Stigler, J., G.O. Camdere, D.E. Koshland, and E.C. Greene. 2016. Single-Molecule Imaging Reveals a Collapsed Conformational State for DNA-Bound Cohesin. *Cell Rep*. 15:988-998.10.1016/j.celrep.2016.04.003

Swartz, R.K., E.C. Rodriguez, and M.C. King. 2014. A role for nuclear envelope-bridging complexes in homology-directed repair. *Mol Biol Cell*. 25:2461-71.10.1091/mbc.E13-10-0569

Symmons, O., V.V. Uslu, T. Tsujimura, S. Ruf, S. Nassari, W. Schwarzer, L. Ettwiller, and F. Spitz. 2014. Functional and topological characteristics of mammalian regulatory domains. *Genome Res*. 24:390-400.10.1101/gr.163519.113

Terakawa, T., S. Bisht, J.M. Eeftens, C. Dekker, C.H. Haering, and E.C. Greene. 2017. The condensin complex is a mechanochemical motor that translocates along DNA. *Science*.10.1126/science.aan6516

Thon, G., P. Bjerling, C.M. Bünner, and J. Verhein-Hansen. 2002. Expression-state boundaries in the mating-type region of fission yeast. *Genetics*. 161:611-22

Tran, P.T., L. Marsh, V. Doye, S. Inoué, and F. Chang. 2001. A mechanism for nuclear positioning in fission yeast based on microtubule pushing. *J Cell Biol*. 153:397-411.10.1083/jcb.153.2.397

Van Bortle, K., and V.G. Corces. 2012. tDNA insulators and the emerging role of TFIIIC in genome organization. *Transcription*. 3:277-84.10.4161/trns.21579

Wang, S., J.H. Su, B.J. Beliveau, B. Bintu, J.R. Moffitt, C.T. Wu, and X. Zhuang. 2016. Spatial organization of chromatin domains and compartments in single chromosomes. *Science*. 353:598-602.10.1126/science.aaf8084

Weber, S.C., A.J. Spakowitz, and J.A. Theriot. 2012. Nonthermal ATP-dependent fluctuations contribute to the in vivo motion of chromosomal loci. *Proc Natl Acad Sci U S A*. 109:7338-43.10.1073/pnas.1119505109

Wendt, K.S., K. Yoshida, T. Itoh, M. Bando, B. Koch, E. Schirghuber, S. Tsutsumi, G. Nagae, K. Ishihara, T. Mishiro, K. Yahata, F. Imamoto, H. Aburatani, M. Nakao, N. Imamoto, K. Maeshima, K. Shirahige, and J.M. Peters. 2008. Cohesin mediates transcriptional insulation by CCCTC-binding factor. *Nature*. 451:796-801.10.1038/nature06634

Zhurinsky, J., S. Salas-Pino, A.B. Iglesias-Romero, A. Torres-Mendez, B. Knapp, I. Flor-Parra, J. Wang, K. Bao, S. Jia, F. Chang, and R.R. Daga. 2019. Effects of the microtubule nucleator Mto1 on chromosomal movement, DNA repair, and sister chromatid cohesion in fission yeast. *Mol Biol Cell*. 30:2695-2708.10.1091/mbc.E19-05-0301

Zimmer, C., and E. Fabre. 2019. Chromatin mobility upon DNA damage: state of the art and remaining questions. *Curr Genet*. 65:1-9.10.1007/s00294-018-0852-6